Machine learning-assisted optimization of multi-metal hydroxide electrocatalysts for overall water splitting

Carina Yi Jing Lim[a], Riko I Made[a], Zi Hui Jonathan Khoo[a,b], Chee Koon Ng[a], Yang Bai[a,c], Jianbiao Wang[a], Gaoliang Yang[a], Albertus D. Handoko[a,b], Yee-Fun Lim[a,b*]*

[a]*Institute of Materials Research and Engineering (IMRE), Agency for Science, Technology and Research (A*STAR), 2 Fusionopolis Way, Innovis, Singapore 138634, Singapore*

[b]*Institute of Sustainability for Chemical, Energy and Environment (ISCE[2]), Agency of Science, Technology and Research (A*STAR), 1 Pesek Road, Singapore 627833, Singapore.*

[c]*Department of Electrical and Computer Engineering, University of Toronto, Toronto, Ontario M5S 3G4, Canada*

**Email: Handoko_Albertus@isce2.a-star.edu.sg*

**Email: limyf@isce2.a-star.edu.sg*

Abstract

Green hydrogen produced via electrochemical water splitting is a suitable candidate to replace emission-intensive fuels. However, the successful widespread adoption of green hydrogen is contingent on the development of low-cost, earth-abundant catalysts. Herein, machine learning models built on experimental data were used to optimize the precursor ratios of hydroxide-based electrocatalysts, with the objective of improving the product's electrocatalytic performance for overall water splitting. The Neural Network-based models were found to be the most effective in predicting and minimizing the overpotentials of the catalysts, reaching a minimum in two iterations. The relatively mild reaction conditions of the synthesis procedure, coupled with its scalability demonstrated herein, renders the optimized catalyst relevant for industrial implementation in the future. The optimized catalyst, characterized to be a molybdate-intercalated CoFe LDH, demonstrated overpotentials of 266 and 272 mV at 10 mA cm^{-2} for oxygen and hydrogen evolution reactions respectively in alkaline electrolyte, alongside unwavering stability for overall water splitting over 50 h. Overall, our results reflect the efficacy and advantages of machine learning strategies to alleviate the time and labour-

intensive nature of experimental optimizations, which can greatly accelerate electrocatalysts research.

New concepts

We demonstrate a relatively straightforward implementation of machine learning for the optimization of synthesis parameters to yield the best-performing catalysts for overall water splitting in a given material space. In contrast to the majority of first-principles based machine learning approaches in the literature, this work highlights how simple machine learning methods can be practically integrated into experimental workflows to expedite electrocatalysis performance optimization. Specifically, we show how the experimental overpotentials of both electrocatalytic hydrogen and oxygen evolution reactions can be correlated directly to the input parameters – namely the molar fractions of the 5 metal-based precursors, leading to rapid performance optimisation. Computationally and experimentally-intensive steps of ascertaining structure-property-performance relations can then be reserved for better performing catalysts. As the machine learning models used herein are open source and easily adaptable, we expect wider implementation of the concept beyond electrocatalysis field.

1. Introduction

Electrochemical water splitting can produce green hydrogen from renewable energy or off-peak surplus electricity, which is poised as a suitable low-carbon alternative to fossil fuels.[1, 2] Unfortunately, existing catalysts for water splitting are dominated by platinum group metals that are both rare and expensive. To accelerate industrial-scale applications, development of efficient and stable bifunctional catalysts based on earth-abundant elements for both half-reactions of water electrolysis is highly desirable.[3, 4] To further reduce manufacturing complexity and cost, the preparation of these electrocatalysts should also be simple and scalable.

Layered double hydroxides (LDHs) are one such class of bifunctional electrocatalysts demonstrating noteworthy overall electrochemical water-splitting activity due to their unique lamellar structure and tuneable compositions.[5] The structure of LDHs may be described as brucite-like metal hydroxide layers, but with 3+ oxidation states metals introduced into the 2+ metal hydroxide host structure, thereby leading to the intercalation of anion between the layers to compensate for additional positive charges.[6] The electrocatalytic performances of these LDH structures have been shown to be further enhanced via diverse strategies including utilizing multi-metallic compositions,[7, 8] doping and defect engineering,[9-12] as well as heterostructures and hierarchical architectures.[13, 14] In addition, it has been reported that introducing different intercalated ions also affect the electrochemical performance of the catalysts. This includes the influence of intercalated electrolyte cations[15] as well as anions introduced into the interlayer spacing during the preparation of the LDH.[16-18] For example, molybdate,[19] and tungstate[20] intercalated nickel-iron (NiFe) LDHs have significantly enhanced oxygen evolution (OER) activities. Systematic compositional studies via high-throughput experimentations have been used to investigate the electrocatalytic activity of complex multi-metallic (oxy)hydroxides.[21,

[22] Alas, such approaches require screening of the entire material space to be fully effective, which remains extremely tedious and relies heavily on costly high-throughput instrumentation.

Beyond the full-scale high-throughput experiments, machine learning (ML)-aided approaches have also garnered increasing attention in electrocatalysis.[23] Many of these ML studies and discussions are centred around computational models and density functional theory (DFT)-based catalyst screening.[24-29] However, it is common to observe a very wide disparity between the theoretically predicted potential and experimental reality, arising from a myriad of factors that remain very challenging to model accurately – such as the synthesis viability, reaction micro-environment, side reactions, and catalyst stability.[30] Whilst there have been many recent advances in ML models based on experimental data for electrocatalysis,[29, 31, 32] none for LDH systems have been reported to our knowledge. Ergo, the objective of this work is to implement a straightforward ML-driven optimization of LDH synthesis for overall water splitting based solely on the elemental composition of the electrocatalyst, with a small initial training dataset generated in-house and efficient convergence towards optimum performance via optimum tuning of the Bayesian Optimization process.[33]

Given the rich literature on NiFe,[6, 13, 34] cobalt-iron (CoFe),[35-37] and NiCoFe[7, 38] LDH-based catalysts and the abovementioned molybdate- and tungstate-intercalated LDHs, we seek an optimized LDH synthesis for overall water splitting centred around these five metal components. Given the five-dimensional material space selected, a typical full-scale optimization approach would be extremely time- and resource-intensive. Rather than approaching catalyst synthesis with a preferred composition and material in mind, we instead allow the ML models to optimize the metal precursor ratios based on the performance of the catalysts alone, facilitating the exploration of the parameter space without human biases. The optimization of the synthesis parameters is entirely based on the experimental electrochemical

performance of the catalysts, bypassing the need to obtain the composition-structure-property relationship of each datapoint. Such a straightforward approach aims to reflect practical implementation of ML in experimental workflows and demonstrate the efficacy of simple ML approaches without the use of extremely large datasets generated by high-throughput set-ups nor computationally-intensive calculations, given that both of which remain inaccessible to many experimentalists.

Despite the relatively small initial dataset of 53 samples, the ML models – particularly that from the Neural Network algorithm – were found to be efficient in optimizing the synthesis of electrocatalysts for overall water splitting. At present, we demonstrate the convergence of the models in as little as two iterations with the Neural Network predictive oracle, with a molybdate-intercalated CoFe hydroxide as the best performing overall electrochemical water splitting catalyst in alkaline conditions, with OER and HER overpotentials of 267 and 272 mV at 10 mA cm^{-2} when deposited on an Ni foam.

2. Results and discussion

A wet-chemistry approach based on NiFe LDH synthesis[39] was adopted in this work. This triethanolamine-assisted route is selected for its mild reaction conditions of 95 °C in aqueous medium, without the need for strict monitoring and control of the solution pH. These mild conditions are amenable to automated workstations while retaining the ease of scaling up toward commercial production in the future. Five metal salts, namely cobalt(II) nitrate hexahydrate, nickel(II) nitrate hexahydrate, iron(III) nitrate nonahydrate, ammonium molybdate (para) tetrahydrate, and ammonium tungsten oxide hydrate were employed as Co, Ni, Fe, Mo, and W metal precursors respectively. Automated synthesis of the catalysts was conducted on a Lissy Chemical Workstation from Zinsser Analytics, which allows for pre-programmed steps of pipetting, shaking, and heating (full synthesis methods in **Section S1.2**).

The synthesized catalysts were then re-dispersed, drop-casted onto glassy carbon electrodes, and tested in a typical three-electrode rotating disc set-up in 1 M potassium hydroxide electrolyte (**Section S1.4**).

2.1. Machine learning optimization of synthesis parameters

The input parameters were chosen to be the molar ratio of the five metal precursors (X). With that the true number and identity of the active sites are difficult to ascertain, we adopt the recommendation where turnover frequency of the catalysts considers all relevant metal sides as active sites.[40] Hence, the molar amount of all metal species – both cationic and anionic – is kept constant. In other words, X represents a set of five molar ratios, each varying between 0 and 1, with the sum of the five ratios equalling to 1.

An initial dataset was constructed by obtaining OER and HER overpotentials at 10 mA cm^{-2} (η_{OER} and η_{HER}) and bifunctional activity metric ($Y_{bifunc.} = -\left({\eta_{OER}}^2 + {\eta_{HER}}^2\right)^{-1}$) from linear sweep voltammetry (LSV) measurement at 10 mV s^{-1} of 53 samples synthesized with random varying ratios of the five metal precursors (**Figure S3.1-3**, samples labelled *i*-{}). The initial dataset is relatively diverse (**Figure S2.7**), with η_{OER} values between 279 to 409 mV; η_{HER} values from 348 to 562 mV; and $Y_{bifunc.}$ values between -2.18 and -4.90.

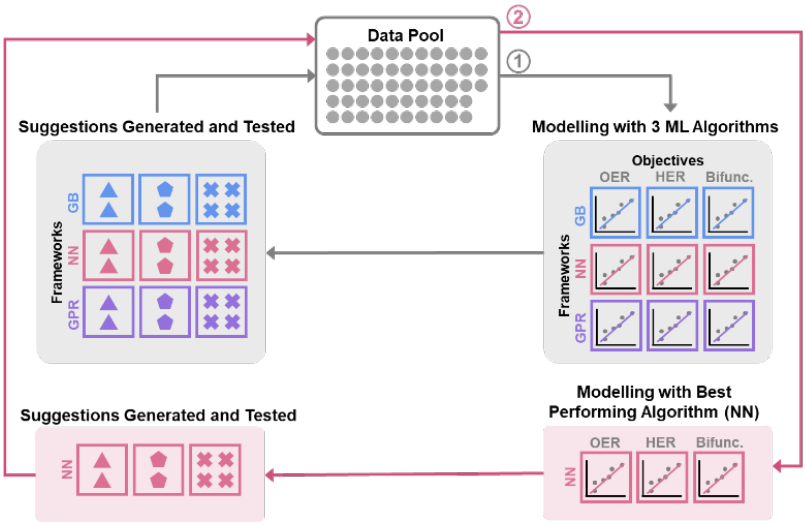

Figure 1. Summary of machine learning optimization workflow.

The overall machine learning workflow is summarised in **Figure 1**. For model construction, we split the datasets into *training* and *test* set with proportion of 70% and 30% of the dataset size respectively (**Figure S2.1**). We applied (trained and hyperparameters optimized) three commonly used machine learning (ML) algorithms, namely Gaussian Process Regression (GPR), Gradient Boosting (GB), and Neural Network (NN) to the dataset. GPR and GB were implemented in Python using *scikit_learn* library,[41] while NN was implemented using *pytorch* library.[42]

We utilized Bayesian-Optimization with Gaussian process surrogate (BO-GP) to search for the optimum set of hyperparameters for each machine learning algorithm. The *gp_minimize* function, implemented in *scikit-optimize*,[43] was used for hyperparameter tuning across the algorithms via minimization of the mean squared error (MSE) of the predictions for a third of the *test* set. The full description of the machine learning methods may be found in **Section S2.1**. The objectives were to optimize the synthesis of electrocatalysts for oxygen evolution reaction (OER), hydrogen evolution reaction (HER), and collectively for both reactions. Machine learning surrogate models for these three objectives were then built for each of the algorithms as follows:

$$\eta_{OER} = f_{OER}(X) \tag{1}$$

$$\eta_{HER} = f_{HER}(X) \tag{2}$$

$$Y_{bifunc.} = -\left({\eta_{OER}}^2 + {\eta_{HER}}^2\right)^{-1} = f_{bifunc.}(X) \tag{3}$$

where X represents the molar ratio of the metal precursors; and f_{OER}, f_{HER}, and $f_{bifunc.}$ are the surrogate functions for η_{OER}, η_{HER}, and $Y_{bifunc.}$, respectively. We opted for a simple negative inverse sum of squares of η_{OER} and η_{HER} to evaluate the overall water splitting performance of the catalyst as opposed to more complex scalarization methods such as Chimera,[44] due to ease of implementation and high sensitivity to small changes in both η_{HER} and η_{OER}. For the optimization, the objectives were set to minimise equations (1), (2), and (3) separately, to

obtain sets of suggested molar ratio of the metal precursors (X^*) via *gp_minimize*. Two X^* for each of the f_{OER} and f_{HER} as well as four X^* for bifunctional catalysts $f_{bifunc.}$ were then synthesized and tested, adding 24 datapoints to the dataset (**Figure S3.4-5**). The uniqueness of the X^* selected with respect to the 53 points of the initial dataset is evaluated by projecting the five-input composition to two transformed axis using Uniform Manifold Approximation and Projection (UMAP, **Section S2.2**, **Figure S2.7**).[45] The ML suggestions are rather distinct and unique from the initial dataset, with the majority of the suggestions lying beyond the UMAP boundary of the initial points. In addition, the UMAP plots reflect a general direction in the UMAP's hyperspace in which the performance of the catalysts seems to improve along, with a significant portion of the ML suggestions crowding in that area of the hyperspace.

Comparing the overpotentials prediction (η_{OER}, η_{HER}, $Y_{bifunc.}$), it is apparent that NN-suggested X^* consistently show much better performance compared to GB and GPR in all objectives (**Figure 2a**). NN also shows the highest prediction accuracy relative to GB and GPR, suggested by the closer datapoints to the parity line across all objectives (**Figure 2b** and **Figure S2.6**). As such, NN was chosen as the preferred technique for subsequent iterations. Interestingly, Ni ratios seem to be suppressed or completely excluded from most of the models' suggestions (**Figure S3.4**), which is contradictory to existing literature on LDH since Ni appears to be central to LDH's water splitting performance.[5] In addition, the GB models also tend to favour higher ratios of W as opposed to the NN suggestions where Mo is preferred.

Combining the additional 24 data points to the initial data set, the NN models were refitted, and new X^* were generated (**Figure S3.6**). Due to significantly higher η_{HER} relative to η_{OER}, reducing η_{HER} has a greater effect in minimizing $Y_{bifunc.}$, consequently leading to similar compositions in the suggestions to minimise η_{HER} and $Y_{bifunc.}$. Similar to the initial iteration, two suggestions each from the $f_{OER}(X)$ and $f_{HER}(X)$ models as well as four suggestions from

the bifunctional model were synthesized and tested (**Figure S3.7**) for each iteration, and all data points were combined into the dataset to be re-fitted in the next iteration.

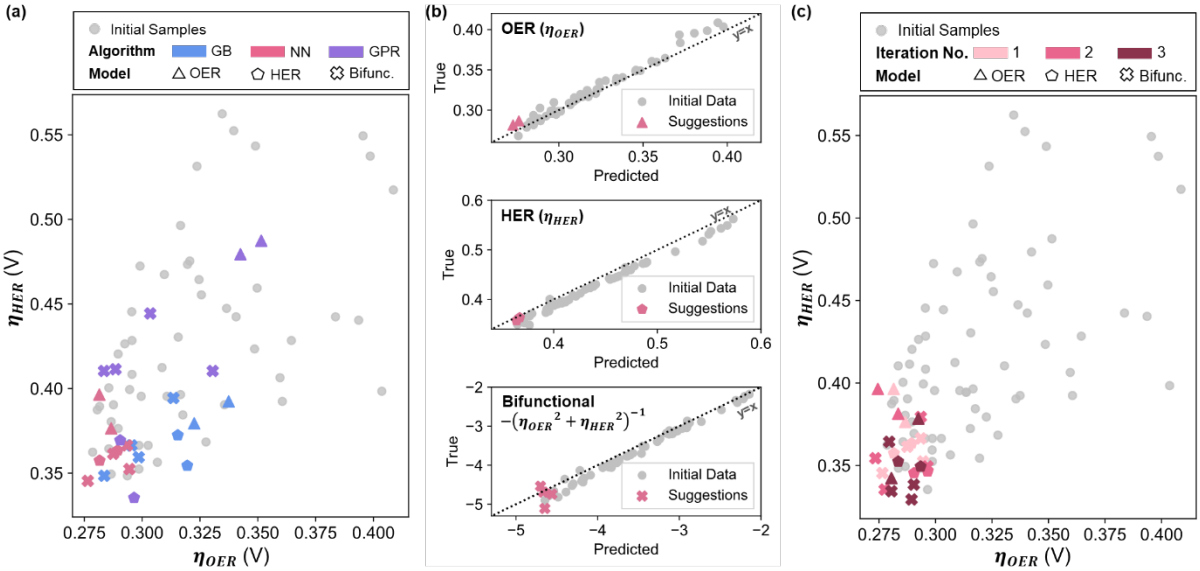

Figure 2. (a) Comparison of experimental η_{HER} and η_{OER} between the initial data set modelled and the performance of the model-suggested compositions of the three ML algorithms. (b) True *vs.* the NN predicted values of the initial dataset alongside the values for the NN-suggested compositions. (c) Experimental η_{HER} and η_{OER} values for the three NN iterations.

After the 3rd iteration, the activities seem to have already converged to a local minimum (**Figure 2c**). NN-12, synthesized with only Co, Fe and Mo precursors from the 2nd NN iteration, was found to have the lowest $Y_{bifunc.}$ value amongst all samples at -5.28. NN-12 has η_{OER} and η_{HER} values of 277.5 mV and 335.4 mV respectively (**Figure 3b-c**). Although NN-12 had the most negative $Y_{bifunc.}$, NN-13 from the 2nd iteration had the overall lowest η_{OER} at 273.4 mV while NN-21 from the 3rd iteration had the lowest η_{HER} at 329.4 mV.

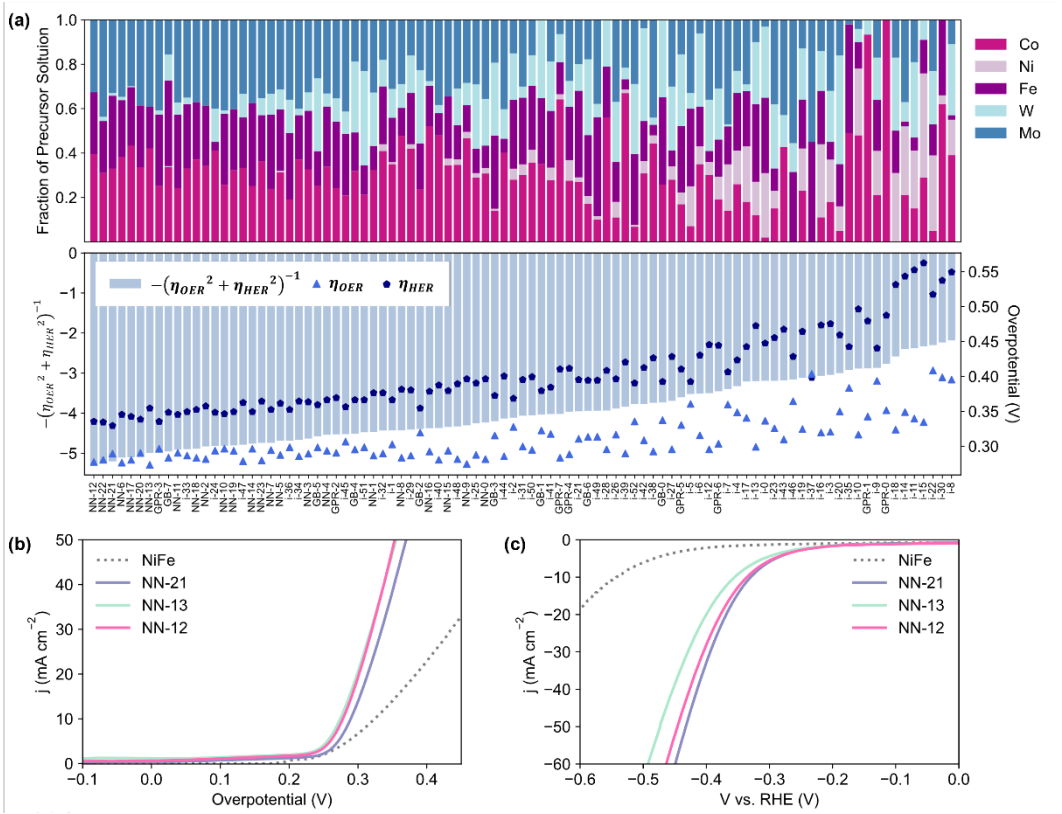

Figure 3. (a) Composition of catalysts synthesized and tested, sorted in order of ascending $Y_{bifunc.}$ and their corresponding $Y_{bifunc.}$, η_{OER}, and η_{HER} values. (b) OER and (c) HER linear sweep voltammograms of the best performing bifunctional (NN-12), HER (NN-21), and OER (NN-13) catalysts, benchmarked against NiFe LDH synthesized as per literature,[39] with comparable η_{OER} to the reported value. Linear sweep voltammograms collected at 10 mV s^{-1} on half-cell rotating disc electrode set-up in Ar-purged 1 M KOH.

We note that the difference between the overpotentials of the 10 best-performing catalysts is less than 25 mV and may be within experimental error. The compositions of these catalysts follow an apparent trend, where lower overpotentials are achieved with catalysts that excludes Ni alongside low to no amounts of W (**Figure 3a**). Consistently high Fe is also favoured, which is unsurprising given that Fe incorporation has been found to significantly increase the activity of Ni/Co(oxy)hydroxides relative to their unary oxides.[46, 47] The exclusion of Ni is unexpected, especially for OER, since typical NiFe systems generally outperform CoFe,[48, 49] and further characterisation and investigation is conducted below to better understand this trend. Nevertheless, the optimized catalyst significantly outperforms similarly-synthesized NiFe LDH which exhibited η_{OER} and η_{HER} values of 324.5 mV and 542.5 mV respectively,

consistent with the η_{OER} reported value for this synthesis method.[39] Additional discussion on the influence of the five metal precursors is included in the Supplementary Information, **Section S2.2**, **Figure S2.8**, based on the NN models' SHapley Additive exPlanations (SHAP) values.[50]

2.2. Characterisation of the optimized catalyst

Both energy dispersive X-ray (EDX) and X-ray photoelectron spectroscopy (XPS) spectra confirm that NN-12 predominantly comprises of Co, Fe, Mo, and O, with trace amounts of N also observed from contaminant TEA or urea decomposition (**Figure S4.1**).

To validate the potential of the synthesis procedure to be translated towards industrial adoption, the synthesis of NN-12 was also scaled up by a factor of 10 from the scale used in the automated workstation (**Section S1.2**). Similar morphologies resembling agglomerated nanosheets were observed from scanning electron micrographs of samples obtained from the automated and scaled-up synthesis method (**Figure 4a-b**). EDX mappings of the two samples also reveal good homogeneity throughout the samples (**Figure S4.3**), with less than 1.25 at.% variation of metal composition difference between the synthesis methods (**Table S5**). High-resolution XPS scans of both samples are also similar (**Figure 4c-f** and **Figure S4.4**), with multiplets corresponding to $Co(OH)_2$ observed in the Co 2p at 780.4, 782.2, 786.0, and 790.4 eV[51, 52] (**Figure 4c**). Meanwhile, the Fe 2p spectra (**Figure 4d**) suggest that the Fe predominantly exists as Fe(III),[53] while a pair of peaks identifies the Mo species as Mo(VI) from the molybdate[54, 55] (**Figure 4e**). In the O 1s range (**Figure 4f**), several peaks are observed: adsorbed water at 533.0 eV; lattice hydroxides at 531.1 eV; and metal-O species at 529.9 eV, which are largely attributed to the molybdate anions.[52, 56] No major change in the metal oxidation states from their precursors is observed, which is expected given the lack of strongly oxidising or reducing precursors.

Fourier transform infrared spectrometry-attenuated total reflectance (FTIR-ATR) spectra of the catalysts (**Figure 4g-h**) corroborates the presence of O-H groups from the XPS O 1s spectra. A broad absorption band, red-shifted from the 3600 cm^{-1} band of free water molecules, is observed around 3370 cm^{-1} and is attributed to the stretching vibrations of the hydroxyl groups of the LDH as well as surface and interlayer water molecules.[57] This is accompanied by a weaker band at 1625 cm^{-1}, assigned to the O-H bending. Strong features associated with the presence of molybdates are also observed around 900 cm^{-1}, most notably bands related to O-Mo-O and M=O at 856 and 926 cm^{-1} respectively.[57, 58] Meanwhile, other peaks at wavenumbers below 800 cm^{-1} are usually attributed to metal-O/-OH bonding.[59, 60]

Interestingly, a well-defined peak at ~1350 cm^{-1}, typically observed for carbonate anion-intercalated LDH structures from the anti-symmetric stretching mode of carbonate,[61-63] is absent. Such a strong peak was reported in the NiFe FTIR spectrum obtained from the synthesis procedure this work was built upon,[39] and was attributed to the intercalation of carbonate anions from urea decomposition to neutralize the positive charge generated by Fe^{3+} substitution within $Ni(OH)_2$. The absence of such a carbonate feature further supports our hypothesis that molybdate anions may be intercalated into the LDH structure, in place of the carbonate anions.

Peaks identified in the Raman spectra (**Figure S4.5**) of both samples are also consistent with the presence of molybdate species seen with FTIR-ATR, with the strongest features at 328 cm^{-1}, 820 cm^{-1}, and 932 cm^{-1} assigned to its bending, asymmetric stretching, and symmetric stretching modes respectively.[64, 65] A weaker peak observed at 523 cm^{-1} is attributed to metal-oxygen vibrations observed for FeOOH[34, 66] or the Co-O (A_g) symmetric stretching mode,[52] and is consistent with the previous spectra for CoFe LDHs.[17, 67]

No differences were apparent between the X-ray diffraction (XRD) patterns of the samples from either synthesis method as well (**Figure S4.6**). Both patterns reflect poor crystallinity and

are comparable to previous reports of molybdate-doped and intercalated NiFe LDHs.[19, 68] A strong (00*l*) peak at ~10° typically observed for regular LDH structures is absent, suggesting lower periodicity in the direction perpendicular to the layers.[19] No XRD peaks belonging to Co(II)- or Fe(III)-molybdate crystals are observed,[69, 70] supporting the case for molybdate ions intercalation between hydroxide sheets as opposed to a composite of molybdate salts and metal hydroxides or alloying.

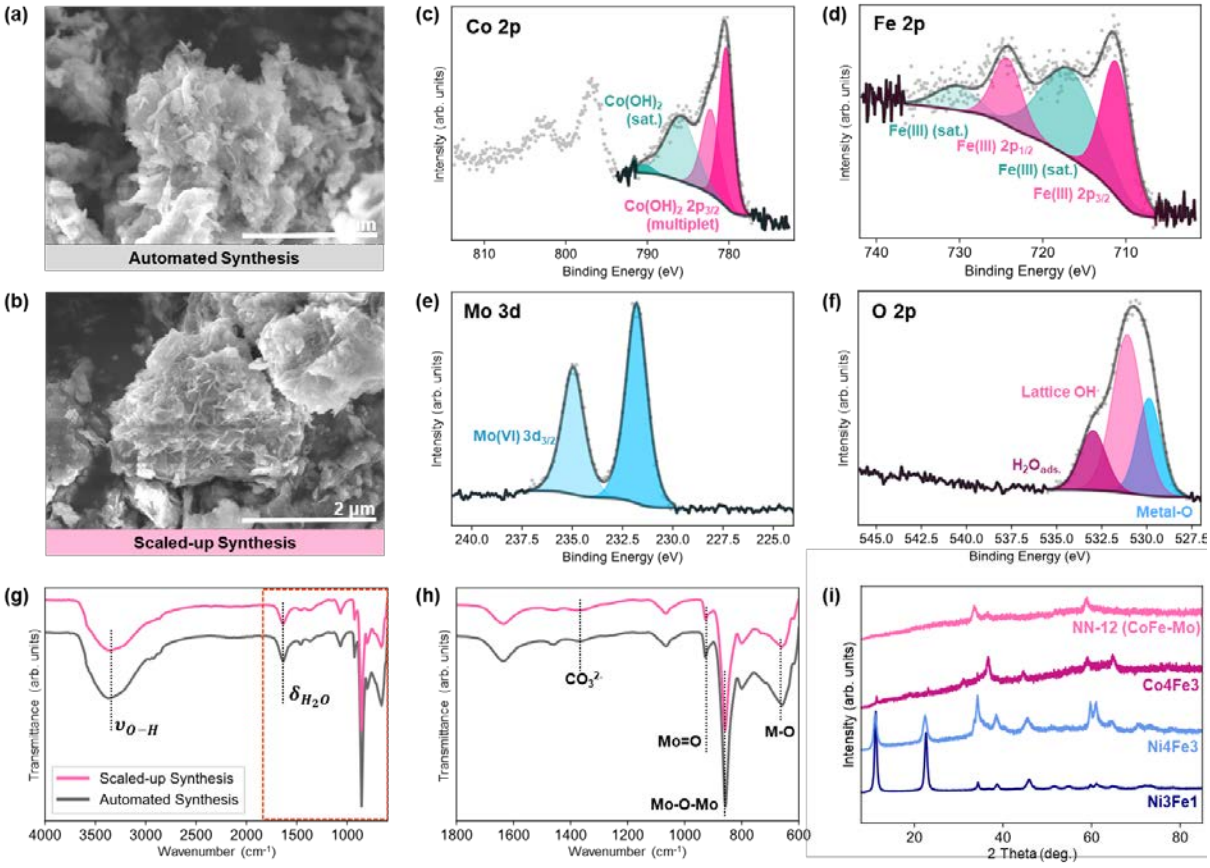

Figure 4. Scanning electron micrographs of NN-12 synthesized via (a) the automated workstation and (b) the scaled-up synthesis. Deconvoluted high-resolution X-ray photoelectron spectra for (c) Co 2p, (d) Fe 2p, (e) Mo 3d, and (f) O 2p of NN-12 synthesized by the automated workstation. (g) Fourier transform infrared spectrometry-attenuated total reflectance spectra of the catalysts and (h) an enlarged portion of the spectra as demarcated by broken lines in (g). (i) X-ray diffraction patterns of NN-12 alongside additional samples with systematic compositional changes,[39] including NiFe from the original synthesis procedure (Ni3Fe1), Ni4Fe3 and Co4Fe3.

Overall, the characterisation of our best catalyst suggests that the ML-optimized parameters yields a molybdate-intercalated CoFe LDH. The promising overall water splitting activity of

this ML-suggested material is consistent with a recent report on Mo-doped CoFe LDH synthesized via electrochemical oxidation of CoFe Prussian-blue nanocubes, demonstrating excellent performance for overall water splitting.[11] Although studies on molybdate-intercalated CoFe are limited, molybdate intercalation into NiFe LDH structures have been widely studied, particularly for improving the electrocatalytic activity for OER. To elaborate, the molybdate species were found to facilitate the reconstruction of the OER-active M-OOH phases,[71-73] by undergoing dissolution and re-adsorption process at OER conditions. Molybdate anions were similarly observed to promote the reconstruction of α-$Co(OH)_2$ nanosheets to active Co-OOH phases,[74] and we posit similar effects may be operating in our NN-12 sample. In addition, prior literature also suggest that Mo doping could induce redistribution of the surface electron density to accelerate charge transfer and promote the formation of the *OOH intermediate for NiFe LDH structures as well.[11, 68, 71, 75] Congruent with these prior observations, NN-12 also exhibits significantly lower charge transfer resistance (R_{ct}) than the original NiFe LDH,[39] as observed from electrochemical impedance spectroscopy (**Figure S5.4**).

To better understand the physical phenomenon behind the ML suggestion, additional samples were synthesised and characterised, varying the Ni:Fe ratio, replacing Ni and Co as well as replacing the molybdate from NN-12 with tungstate. As mentioned, the (00*l*) peak reflects the stacking order of the catalysts. It was found that the incorporation of Co, exacerbated by the high Fe content and molybdate incorporation, compromises the crystallinity and stacking order of the LDH as shown from the diminishing (00*l*) peak (**Figure 4i**). Given that the stability of the bulk LDH structure has been found to be affected by interlayer anions,[76] the incorporation of molybdate may decrease the cohesion between the LDH sheets, leading to the disruption of the turbostratic structure. Relative to well stacked layers, structures with poor crystallinity and stacking have increased surface area, exposure of rich active sites as well as defects, all of which may contribute to enhanced electrochemical activity.[77, 78] Meanwhile, the incorporation

of tungstate seems to induce the precipitation of electrically insulating FeOOH phase (**Figure S4.7**), which degrades the electrochemical performance. The full discussion may be found in the Supplementary Information, **Section S4.2**. Overall, despite the NiFe LDH is expected to have higher OER activity than CoFe LDH in the literature,[48] we hypothesise that the intrinsic activities of the materials may be outweighed by the influence of the catalysts' nanostructures arising from synthesis method variation.

2.3. Catalyst Stability

To better reflect the performance of the catalyst in practical applications, NN-12 from the scaled-up synthesis procedure was also tested on larger stationary electrodes, where the catalysts are air-brushed onto both sides of 0.3 mm Ni foams (**Section S1.4**). Electrode areas measuring 1×1 cm (geometric active area = 2 cm^2 per electrode) were isolated using epoxy resin to minimise possible current contributions from electrolyte ingress.

Half-cell chronopotentiometry of NN-12/Ni foam electrodes was conducted at 10 mA cm_{geo}^{-2}, delivering overpotentials of 266 and 272 mV for OER and HER respectively (averaged from the 2^{nd} to 10^{th} hour, **Figures 5a and 5c**). Higher initial overpotentials observed is common amongst similar catalysts,[79] and may be attributed to the ongoing reconstruction of the catalysts as these foam electrodes are not pre-treated. Apart from the formation of active metal hydroxide phases,[48, 80] the reconstruction process may also include dynamic dissolution and re-adsorption of the molybdate anions[71-74, 81] as mentioned earlier. No significant degradation was observed from LSV measured after 10 h (**Figures 5b and 5d**), alluding to the good long-term stability of the catalyst. In addition, the observed OER Tafel slope of 59 mV dec^{-1} (**Figure S5.2a**) is in agreement with the proposed mechanisms for alkaline conditions, with reaction kinetics limited by the coverage of M*OOH sites.[82] Meanwhile, the Tafel slope value for HER of 170 mV dec^{-1} (**Figure S5.2b**) is comparable to prior literature of LDH-based catalysts with no heteroatom

doping.[83] The deviation from cardinal HER Tafel values suggests possible Volmer-Heyrovsky mechanism,[83, 84] coupled with higher *H coverage and pH effects.[82]

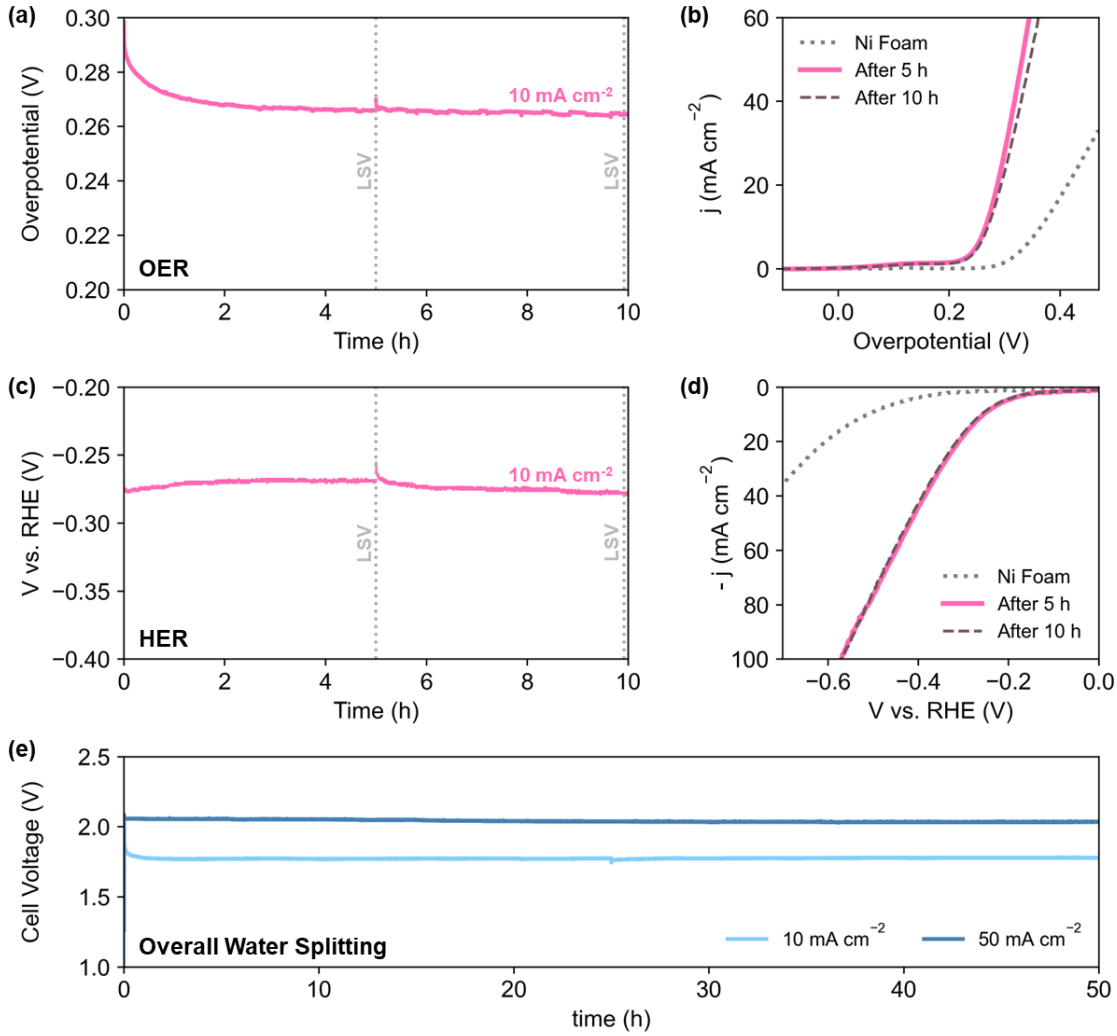

Figure 5. (a) OER chronopotentiometry plot of NN-12/Ni foam at 10 mA cm_{geo}^{-2} and (b) corresponding LSV at 5 mV s^{-1} after 5 and 10 h. (c) HER chronopotentiometry plot of NN-12/Ni foam at 10 mA cm_{geo}^{-2} and (d) corresponding LSV at 5 mV s^{-1} after 5 and 10 h. (e) Chronopotentiometry runs of the electrode tested for overall water splitting at current densities of 10 mA cm_{geo}^{-2} and 50 mA cm_{geo}^{-2} for 50 hours. Electrolyte: Ar-purged 1 M KOH.

The performance for overall water splitting was also evaluated via chronopotentiometry with the NN-12/Ni foam electrodes serving as both the cathode and anode. At 10 and 50 mA cm_{geo}^{-2}, the cell voltage stabilised at around 1.78 and 2.04 V respectively, with no significant loss of activity after 50 h. Further quantification of hydrogen gas evolved during HER via gas chromatography yields average Faradaic efficiency of 99.5% over more than 4 h at 10 mA cm-

^{2} (**Figure S5.3**). Given its simple synthesis and structure, with no further modifications nor dopants, NN-12 delivers respectable performance and catalytic durability for overall water splitting, with comparable catalytic activities to some of the best LDH catalysts from prior literature (**Table S6**).

3. Conclusion

In summary, we demonstrate the optimization of a simple synthesis and scalable procedure for bifunctional water splitting electrocatalysts. An optimum composition with the lowest bifunctional overpotential was found with merely two experimental iterations of our machine learning workflow. The syntheses were conducted in an automated workstation and the optimization was driven via ML through NN models built upon experimental data of 53 samples. The best-performing catalyst, NN-12, was tested to possess the characteristics of molybdate-intercalated CoFe LDHs, alongside good activity and stability for overall water splitting. Nevertheless, there remains much room for improvement and exploration in this work, such as increasing the material space and input parameters to be optimized. Possible expansion of this work includes the optimisation of heteroatom dopant species and content, with prior literature reporting promising electrocatalytic[85-88] and photoelectrocatalytic[88, 89] water splitting activity with late transition metal dopants, especially copper and zinc.

Consideration of experimental uncertainty as well as predicted uncertainty in the models may also allow for more robust ML models.[90] In addition, whilst a simple negative inverse sum of squares approach was used herein to optimize for overall water splitting, there also exists well-established methods for multi-objective optimizations such as Chimera,[44] which are particularly suited for more complex multi-objective optimizations.

Our key message is to highlight the efficacy of ML in assisting the optimization of experimental parameters and encourage experimentalists to tap into ML-assisted workflows to accelerate the

time and labour-intensive nature of experimental work – particularly those with numerous parameters to be simultaneously optimized. Moreover, the use of ML may also aid in material discovery by removing human biases from the experimental process. Herein, the exclusion of Ni surprisingly led to better catalytic performances – which would not have been otherwise considered based on our preconception that Ni-based LDHs would yield better performances than Co-based LDHs. Other methods such as Phoenics[91] have also been developed with chemistry and experimentation in mind, which is also an incredible tool for experimental catalyst discovery and optimization. Nevertheless, there remain many areas for further development. For example, developing better models suitable for smaller datasets would further increase the accessibility of ML to experimentalists, particularly for experiments conducted without high-throughput or automated set-ups to generate large data volumes. Such machine learning methods may be further expanded upon to facilitate the discovery and optimization of electrocatalysts over a wider material space, with greater efficiency relative to the *Edisonian* approach typically adopted in experimental catalysis research.

Acknowledgements

This work is supported by the Agency for Science, Technology and Research (A*STAR), and carried out within the framework of the Accelerated Catalysis Development Platform (grant number A19E9a0103).

The authors acknowledge Dr Debbie Seng Hwee Leng, Dr Jian Liang Cheong and Dr Sebastian Yongsen Quek for their assistance in XPS and ATR-FTIR measurements.

Code Availability

Code available upon reasonable request.

Conflict of Interest Statement

The authors declare no competing interests.

References

1 M. Noussan, P. P. Raimondi, R. Scita and M. Hafner, *Sustainability*, 2020, **13**, 298.
2 X. Fu, R. Shi, S. Jiao, M. Li and Q. Li, *Journal of Energy Chemistry*, 2022, **70**, 129-153.
3 J. Wang, X. Yue, Y. Yang, S. Sirisomboonchai, P. Wang, X. Ma, A. Abudula and G. Guan, *J. Alloys Compd.*, 2020, **819**, 153346.
4 B. You and Y. Sun, *Acc. Chem. Res.*, 2018, **51**, 1571-1580.
5 Y. Wang, D. Yan, S. El Hankari, Y. Zou and S. Wang, *Adv. Sci.*, 2018, **5**, 1800064.
6 F. Dionigi and P. Strasser, *Adv. Energy Mater.*, 2016, **6**, 1600621.
7 M. Oliver-Tolentino, J. Vazquez-Samperio, M. Tufiño-Velázquez, J. Flores-Moreno, L. Lartundo-Rojas and R. de G. Gonzalez-Huerta, *J. Appl. Electrochem.*, 2018, **48**, 947-957.
8 F. Qin, Z. Zhao, M. K. Alam, Y. Ni, F. Robles-Hernandez, L. Yu, S. Chen, Z. Ren, Z. Wang and J. Bao, *ACS Energy Lett.*, 2018, **3**, 546-554.
9 H. S. Jadhav, A. Roy, B. Z. Desalegan and J. G. Seo, *Sustainable Energy & Fuels*, 2020, **4**, 312-323.
10 P. F. Liu, S. Yang, B. Zhang and H. G. Yang, *ACS Appl. Mater. Interfaces*, 2016, **8**, 34474-34481.
11 G. Zhao, B. Wang, Q. Yan and X. Xia, *J. Alloys Compd.*, 2022, **902**, 163738.
12 H. Sun, L. Chen, Y. Lian, W. Yang, L. Lin, Y. Chen, J. Xu, D. Wang, X. Yang, M. H. Rümmerli, J. Guo, J. Zhong, Z. Deng, Y. Jiao, Y. Peng and S. Qiao, *Adv. Mater.*, 2020, **32**, 2006784.
13 Y. Ma, D. Liu, H. Wu, M. Li, S. Ding, A. S. Hall and C. Xiao, *ACS Appl. Mater. Interfaces*, 2021, **13**, 26055-26063.
14 Y. Tang, Q. Liu, L. Dong, H. B. Wu and X.-Y. Yu, *Appl. Catal., B.*, 2020, **266**, 118627.
15 J. Zaffran, M. B. Stevens, C. D. M. Trang, M. Nagli, M. Shehadeh, S. W. Boettcher and M. Caspary Toroker, *Chem. Mater.*, 2017, **29**, 4761-4767.
16 D. Zhou, Z. Cai, Y. Bi, W. Tian, M. Luo, Q. Zhang, Q. Zhang, Q. Xie, J. Wang, Y. Li, Y. Kuang, X. Duan, M. Bajdich, S. Siahrostami and X. Sun, *Nano Res.*, 2018, **11**, 1358-1368.
17 G. Xiao, W. Chen, Y. Cai, S. Zhang, D. Wang and D. Cai, in *Catalysts*, 2022.

18 B. M. Hunter, W. Hieringer, J. R. Winkler, H. B. Gray and A. M. Müller, *Energy Environ. Sci.*, 2016, **9**, 1734-1743.
19 N. Han, F. Zhao and Y. Li, *J. Mater. Chem. A*, 2015, **3**, 16348-16353.
20 X. Xue, F. Yu, B. Peng, G. Wang, Y. Lv, L. Chen, Y. Yao, B. Dai, Y. Shi and X. Guo, *Sustainable Energy & Fuels*, 2019, **3**, 237-244.
21 J. A. Haber, C. Xiang, D. Guevarra, S. Jung, J. Jin and J. M. Gregoire, *ChemElectroChem*, 2014, **1**, 524-528.
22 J. B. Gerken, S. E. Shaner, R. C. Massé, N. J. Porubsky and S. S. Stahl, *Energy Environ. Sci.*, 2014, **7**, 2376-2382.
23 G. H. Gu, J. Noh, I. Kim and Y. Jung, *J. Mater. Chem. A*, 2019, **7**, 17096-17117.
24 M. Karthikeyan, D. M. Mahapatra, A. S. A. Razak, A. A. M. Abahussain, B. Ethiraj and L. Singh, *Catalysis Reviews*, 2022, 1-31.
25 L. Chen, X. Zhang, A. Chen, S. Yao, X. Hu and Z. Zhou, *Chinese Journal of Catalysis*, 2022, **43**, 11-32.
26 N. K. Pandit, D. Roy, S. C. Mandal and B. Pathak, *J. Phys. Chem. Lett.*, 2022, **13**, 7583-7593.
27 L. Chen, Y. Tian, X. Hu, S. Yao, Z. Lu, S. Chen, X. Zhang and Z. Zhou, *Adv. Funct. Mater.*, 2022, **32**, 2208418.
28 X. Zhang, Y. Tian, L. Chen, X. Hu and Z. Zhou, *J. Phys. Chem. Lett.*, 2022, **13**, 7920-7930.
29 H. Mai, T. C. Le, D. Chen, D. A. Winkler and R. A. Caruso, *Chem. Rev.*, 2022, **122**, 13478-13515.
30 J. Resasco, F. Abild-Pedersen, C. Hahn, Z. Bao, M. T. M. Koper and T. F. Jaramillo, *Nat. Catal.*, 2022, **5**, 374-381.
31 A. Zheng, Y. Wang, F. Zhang, C. He, S. Zhu and N. Zhao, *iScience*, 2021, **24**, 103430.
32 M. R. Karim, M. Ferrandon, S. Medina, E. Sture, N. Kariuki, D. J. Myers, E. F. Holby, P. Zelenay and T. Ahmed, *ACS Appl. Energy Mater.*, 2020, **3**, 9083-9088.
33 Y.-F. Lim, C. K. Ng, U. S. Vaitesswar and K. Hippalgaonkar, *Advanced Intelligent Systems*, 2021, **3**, 2100101.
34 Z. Qiu, C.-W. Tai, G. A. Niklasson and T. Edvinsson, *Energy Environ. Sci.*, 2019, **12**, 572-581.
35 R. Yang, Y. Zhou, Y. Xing, D. Li, D. Jiang, M. Chen, W. Shi and S. Yuan, *Appl. Catal., B.*, 2019, **253**, 131-139.
36 D. S. Patil, S. A. Pawar, S. H. Lee and J. C. Shin, *J. Electroanal. Chem.*, 2020, **862**, 114012.
37 L. Feng, A. Li, Y. Li, J. Liu, L. Wang, L. Huang, Y. Wang and X. Ge, *ChemPlusChem*, 2017, **82**, 483-488.
38 A. T. N. Nguyen, M. Kim and J. H. Shim, *RSC Adv.*, 2022, **12**, 12891-12901.
39 S. Jaśkaniec, C. Hobbs, A. Seral-Ascaso, J. Coelho, M. P. Browne, D. Tyndall, T. Sasaki and V. Nicolosi, *Sci. Rep.*, 2018, **8**, 4179.
40 F. Song, L. Bai, A. Moysiadou, S. Lee, C. Hu, L. Liardet and X. Hu, *J. Am. Chem. Soc.*, 2018, **140**, 7748-7759.
41 F. Pedregosa, G. Varoquaux, A. Gramfort, V. Michel, B. Thirion, O. Grisel, M. Blondel, P. Prettenhofer, R. Weiss, V. Dubourg, J. Vanderplas, A. Passos, D. Cournapeau, M. Brucher, M. Perrot, E. Duchesnay and G. Louppe, *Journal of Machine Learning Research*, 2011, **12**, 2825-2830.
42 A. Paszke, S. Gross, F. Massa, A. Lerer, J. Bradbury, G. Chanan, T. Killeen, Z. Lin, N. Gimelshein, L. Antiga, A. Desmaison, A. Köpf, E. Z. Yang, Z. DeVito, M. Raison, A. Tejani, S. Chilamkurthy, B. Steiner, L. Fang, J. Bai and S. Chintala, in *33rd Conference on Neural Information Processing Systems*, eds. H. Wallach, H. Larochelle, A. Beygelzimer, F. d'Alché-Buc, E. Fox and R. Garnett, Curran Associates, Inc., Vancouver, Canada, 2019, pp. 8024-8035.
43 T. Head, MechCoder, G. Louppe, I. Shcherbatyi, fcharras, Z. Vinícius, cmmalone, C. Schröder, nel, N. Campos, T. Young, S. Cereda, T. Fan, r. rene, K. Shi, J. Schwabedal, carlosdanielcsantos, L. Hvass, M. Pak, SoManyUsernamesTaken, F. Callaway, L. Estève, L. Besson, M. Cherti, K. Pfannschmidt, F. Linzberger, C. Cauet, A. Gut, A. Mueller and A. Fabisch, 2018.
44 F. Häse, L. M. Roch and A. Aspuru-Guzik, *Chem. Sci.*, 2018, **9**, 7642-7655.

45 L. McInnes, J. Healy and J. Melville, *arXiv preprint arXiv:1802.03426*, 2018.
46 M. B. Stevens, L. J. Enman, E. H. Korkus, J. Zaffran, C. D. M. Trang, J. Asbury, M. G. Kast, M. C. Toroker and S. W. Boettcher, *Nano Res.*, 2019, **12**, 2288-2295.
47 M. S. Burke, M. G. Kast, L. Trotochaud, A. M. Smith and S. W. Boettcher, *J. Am. Chem. Soc.*, 2015, **137**, 3638-3648.
48 F. Dionigi, Z. Zeng, I. Sinev, T. Merzdorf, S. Deshpande, M. B. Lopez, S. Kunze, I. Zegkinoglou, H. Sarodnik, D. Fan, A. Bergmann, J. Drnec, J. F. D. Araujo, M. Gliech, D. Teschner, J. Zhu, W.-X. Li, J. Greeley, B. R. Cuenya and P. Strasser, *Nat. Commun.*, 2020, **11**, 2522.
49 M. Chatenet, B. G. Pollet, D. R. Dekel, F. Dionigi, J. Deseure, P. Millet, R. D. Braatz, M. Z. Bazant, M. Eikerling, I. Staffell, P. Balcombe, Y. Shao-Horn and H. Schäfer, *Chem. Soc. Rev.*, 2022, **51**, 4583-4762.
50 S. M. Lundberg and S.-I. Lee, in *31st Conference on Neural Information Processing Systems (NIPS)*, eds. U. v. Luxburg, I. Guyon, S. Bengio, H. Wallach and R. Fergus, Curran Associates Inc., Long Beach, CA, USA, 2017, pp. 4768–4777.
51 M. C. Biesinger, B. P. Payne, A. P. Grosvenor, L. W. M. Lau, A. R. Gerson and R. S. C. Smart, *Appl. Surf. Sci.*, 2011, **257**, 2717-2730.
52 J. Yang, H. Liu, W. N. Martens and R. L. Frost, *J. Phys. Chem. C*, 2010, **114**, 111-119.
53 T. Yamashita and P. Hayes, *Appl. Surf. Sci.*, 2008, **254**, 2441-2449.
54 Y. Lu, M. Zhao, R. Luo, Q. Yu, J. Lv, W. Wang, H. Yan, T. Peng, X. Liu and Y. Luo, *J. Solid State Electrochem.*, 2018, **22**, 657-666.
55 Z.-Q. Liu, L.-Y. Tang, N. Li, K. Xiao, J. Wang, J.-H. Zhang, Y.-Z. Su and Y.-X. Tong, *J. Electrochem. Soc.*, 2012, **159**, D582.
56 J.-C. Dupin, D. Gonbeau, P. Vinatier and A. Levasseur, *Phys. Chem. Chem. Phys.*, 2000, **2**, 1319-1324.
57 K. Nejati, A. R. Akbari, S. Davari, K. Asadpour-Zeynali and Z. Rezvani, *New J. Chem.*, 2018, **42**, 2889-2895.
58 R. Zăvoianu, R. Bîrjega, O. D. Pavel, A. Cruceanu and M. Alifanti, *Appl. Catal. A*, 2005, **286**, 211-220.
59 D. Sun, C. Li, S. Lu, Q. Yang and C. He, *RSC Adv.*, 2021, **11**, 20258-20267.
60 S. Lee, M. Govindan and D. Kim, *Chem. Eng. J.*, 2021, **416**, 127918.
61 T. S. Munonde, H. Zheng and P. N. Nomngongo, *Ultrason. Sonochem.*, 2019, **59**, 104716.
62 F. Z. Mahjoubi, A. Khalidi, M. Abdennouri and N. Barka, *Journal of Taibah University for Science*, 2017, **11**, 90-100.
63 M. Yasaei, M. Khakbiz, E. Ghasemi and A. Zamanian, *Appl. Surf. Sci.*, 2019, **467-468**, 782-791.
64 R. L. Frost, A. W. Musumeci, W. N. Martens, M. O. Adebajo and J. Bouzaid, *J. Raman Spectrosc.*, 2005, **36**, 925-931.
65 J. Wu, Z. Wang, S. Li, S. Niu, Y. Zhang, J. Hu, J. Zhao and P. Xu, *Chem. Commun.*, 2020, **56**, 6834-6837.
66 K. Zhu, J. Chen, W. Wang, J. Liao, J. Dong, M. O. L. Chee, N. Wang, P. Dong, P. M. Ajayan, S. Gao, J. Shen and M. Ye, *Adv. Funct. Mater.*, 2020, **30**, 2003556.
67 E. Musella, I. Gualandi, E. Scavetta, A. Rivalta, E. Venuti, M. Christian, V. Morandi, A. Mullaliu, M. Giorgetti and D. Tonelli, *J. Mater. Chem. A*, 2019, **7**, 11241-11249.
68 Z. Yin, X. Liu, M. Cui, Z. Cao, A. Liu, L. Gao, T. Ma, S. Chen and Y. Li, *Materials Today Sustainability*, 2022, **17**, 100101.
69 G. Harichandran, S. Radha, J. Yesuraj and B. Muthuraaman, *Appl. Phys. A*, 2021, **127**, 627.
70 H. Oudghiri-Hassani, *Catal. Commun.*, 2015, **60**, 19-22.
71 Y. Gan, Y. Ye, X. Dai, X. Yin, Y. Cao, R. Cai and X. Zhang, *J. Colloid Interface Sci.*, 2023, **629**, 896-907.
72 H. Liao, X. Zhang, S. Niu, P. Tan, K. Chen, Y. Liu, G. Wang, M. Liu and J. Pan, *Appl. Catal., B.*, 2022, **307**, 121150.
73 J. Liu, P. Ding, Z. Zhu, W. Du, X. Xu, J. Hu, Y. Zhou and H. Zeng, *Small*, 2021, **17**, 2101671.

74 Y.-L. Meng, Y. Li, Z. Tan, X. Chen, L.-L. Wu, L.-W. Ji, Q.-S. Wang, X.-Z. Song and S. Song, *Energy & Fuels*, 2021, **35**, 2775-2784.
75 Y. Gan, Z. Li, Y. Ye, X. Dai, F. Nie, X. Yin, Z. Ren, B. Wu, Y. Cao, R. Cai, X. Zhang and W. Song, *ChemSusChem*, 2022, **15**, e202201205.
76 J. Zaffran, M. Nagli, M. Shehadeh and M. C. Toroker, *Theor. Chem. Acc.*, 2017, **137**, 3.
77 P. M. Bodhankar, P. B. Sarawade, G. Singh, A. Vinu and D. S. Dhawale, *J. Mater. Chem. A*, 2021, **9**, 3180-3208.
78 F. Song and X. Hu, *Nat. Commun.*, 2014, **5**, 4477.
79 L. Trotochaud, J. K. Ranney, K. N. Williams and S. W. Boettcher, *J. Am. Chem. Soc.*, 2012, **134**, 17253-17261.
80 X. Liu, J. Meng, K. Ni, R. Guo, F. Xia, J. Xie, X. Li, B. Wen, P. Wu, M. Li, J. Wu, X. Wu, L. Mai and D. Zhao, *Cell Reports Physical Science*, 2020, **1**, 100241.
81 Y. Wang, Y. Zhu, S. Zhao, S. She, F. Zhang, Y. Chen, T. Williams, T. Gengenbach, L. Zu, H. Mao, W. Zhou, Z. Shao, H. Wang, J. Tang, D. Zhao and C. Selomulya, *Matter*, 2020, **3**, 2124-2137.
82 T. Shinagawa, A. T. Garcia-Esparza and K. Takanabe, *Sci. Rep.*, 2015, **5**, 13801.
83 H. Yang, Z. Zhou, H. Yu, H. Wen, R. Yang, S. Peng, M. Sun and L. Yu, *J. Colloid Interface Sci.*, 2023, **636**, 11-20.
84 H. Chen, X. Liang, Y. Liu, X. Ai, T. Asefa and X. Zou, *Adv. Mater.*, 2020, **32**, 2002435.
85 J. Han, J. Zhang, T. Wang, Q. Xiong, W. Wang, L. Cao and B. Dong, *ACS Sustain. Chem. Eng.*, 2019, **7**, 13105-13114.
86 L. Yan, B. Zhang, Z. Liu and J. Zhu, *Chem. Eng. J.*, 2021, **405**, 126198.
87 H. Wang, X. Liu, G. Liu, Y. Wang, X. Du and J. Li, *Chem Catalysis*, 2023, **3**, 100552.
88 J. Zaffran and M. C. Toroker, *ChemPhysChem*, 2016, **17**, 1630-1636.
89 J. Zaffran and M. C. Toroker, *ChemistrySelect*, 2016, **1**, 911-916.
90 F. Strieth-Kalthoff, F. Sandfort, M. H. S. Segler and F. Glorius, *Chem. Soc. Rev.*, 2020, **49**, 6154-6168.
91 F. Häse, L. M. Roch, C. Kreisbeck and A. Aspuru-Guzik, *ACS Cent. Sci.*, 2018, **4**, 1134-1145.

For Table of Contents Only